ACS APPLIED MATERIALS & INTERFACES

www.acsami.org

Research Article

Tailoring sp^2-Cluster Distribution to Suppress Corrosion at Amorphous Carbon/Bipolar Plates Interfaces

Hao Li, Jingyun Feng, Peng Guo,* Keiji Komatsu, Rende Chen, Guanshui Ma, Hidetoshi Saito, and Aiying Wang*

Cite This: *ACS Appl. Mater. Interfaces* 2026, 18, 36164−36176

Read Online

ACCESS | Metrics & More | Article Recommendations | Supporting Information

ABSTRACT: With high electrical conductivity and strong corrosion resistance, amorphous carbon (a-C) films are essential for ensuring the durability of metallic bipolar plates (BPs) in proton exchange membrane fuel cells (PEMFCs). However, due to the lack of plasma diagnostics and in situ electrochemical characterization, it is challenging to reveal the real-time corrosion process and to provide theoretical guidance for a-C-coated BPs. Here, we demonstrate a novel approach integrating a rotatable magnetic field with magnetron sputtering to fabricate a-C films under optimized plasma distributions. Results show that varying the magnetic field rotation angle (−60° to 90°) alters the unbalanced coefficient, plasma potential, and electron density. While the sp^2/sp^3-C ratio remained constant across films, the sp^2 cluster diameter changed significantly. The a-C film deposited at 30° exhibited the largest sp^2 cluster (L_a = 1.89 nm). Crucially, BPs coated with this 30° film demonstrated exceptional long-term corrosion resistance during 48 h cathodic/anodic polarization, with interfacial contact resistances of only 2.4 mΩ·cm^2 before corrosion and 3.5 mΩ·cm^2 after corrosion. In situ electrochemical impedance spectroscopy and scanning vibrating electrode technique analysis confirmed that performance degradation stems from localized galvanic corrosion initiation and subsequent corrosion product formation at the interface. This study emphasizes controlling sp^2 clustering and density as a key design principle for enhancing a-C film durability on BPs and advances practical protective film development for PEMFCs.

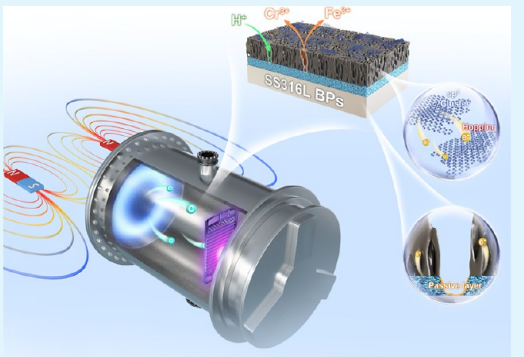

KEYWORDS: *amorphous carbon, interfacial corrosion, sp^2 cluster diameter, magnetic rotation angle, metallic bipolar plates*

1. INTRODUCTION

Proton exchange membrane fuel cells (PEMFCs) have emerged as a leading technology for fuel cell application owing to their quick start-up time, low operational temperature, and high energy density.[1,2] Metallic bipolar plates (BPs) play a crucial role in PEMFCs, serving to separate the oxidant and reductant, conduct current, and support the membrane electrode in order to maintain the stability of the cell stack structure.[3] Despite the fact that commonly used stainless steel, Ti alloy, and Al alloy BPs exhibit good corrosion resistance, the exposure to acidic (pH = 2−3) and high-temperature (60−80 °C) environments within PEMFCs can still lead to the dissolution of metal ions and the formation of oxide layers on the metallic BPs.[4] As a result, the performance of the BPs deteriorates and their service life is shortened.[5]

Recently, a multitude of films have been utilized for the protection of metallic BPs, including noble metal films, metal nitride films, metal oxide films, carbon-based films, and MAX-phase films.[6−8] Specifically, amorphous carbon (a-C) films have garnered significant attention from both the academia and industry due to their exceptional chemical inertness, superb mechanical properties, high conductivity, and cost-effectiveness for large-scale production.[9] These films have been integrated into the hydrogen-powered fuel cell electric car Mirai by Toyota.[10]

Previous research has suggested that a higher sp^2/sp^3 ratio, a larger sp^2 cluster diameter, and lower hydrogen content are key factors for achieving the high conductivity and corrosion resistance of a-C films.[6,11] Primarily, from the perspective of a-C preparation, various parameters during the deposition process, such as temperature, working pressure, sputtering power, and substrate bias, have been explored to optimize performance.[12,13] It is worth noting that specific deposition parameters correspond to distinct states and distributions of plasma, which significantly influence the growth process and microstructure of the a-C film.[14−19] In the case of typical magnetron sputtering, changes in magnetic and electric fields can greatly impact plasma discharge characteristics, particularly plasma density and ion kinetic energy.[20,21] Therefore, adjusting

Received: February 12, 2026
Revised: June 12, 2026
Accepted: June 17, 2026
Published: June 22, 2026

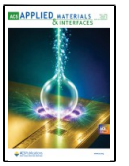

https://doi.org/10.1021/acsami.6c03124
ACS Appl. Mater. Interfaces 2026, 18, 36164−36176

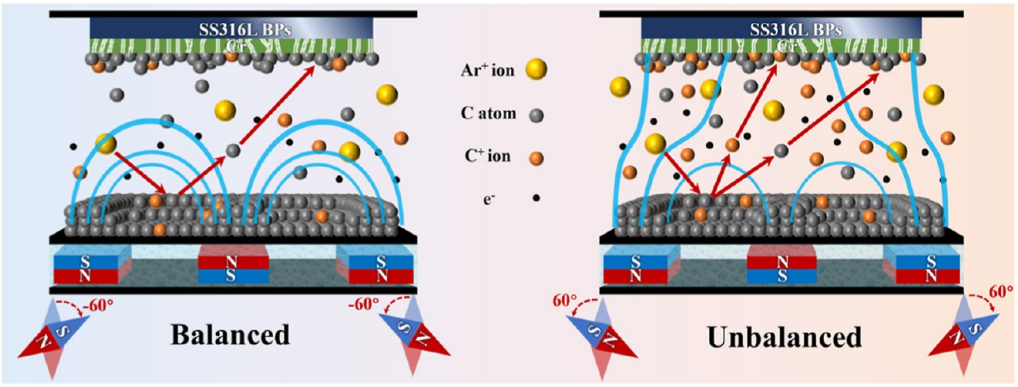

Figure 1. Schematic diagram of magnetron sputtering deposition with a rotatable magnetic field.

the intensity and distribution of the magnetic field may serve as an effective and straightforward strategy for obtaining optimized a-C films.[22] Furthermore, regarding the damage mechanism, galvanic coupling between metallic BPs and a-C can induce significant performance degradation, particularly under high potentials.[12,13,23] However, conventional electrochemical tests are limited to capturing the initial and final corrosion states, thereby failing to reveal the initiation and propagation processes of localized corrosion.[24]

Currently, owing to the absence of plasma diagnostics during deposition and in situ electrochemical characterization, establishing the relationship between plasma conditions, the film microstructure, and the real-time corrosion process of a-C-coated BPs remains challenging. Further research is imperative to establish the theoretical foundation necessary for designing high-performance a-C coatings capable of enduring long-term service environments.

In this study, a rotatable-angle magnetic field was utilized in the magnetron sputtering source to control the magnetic field distribution, leading to the preparation of a series of a-C films on 316L stainless steel (SS316L) substrates. The plasma state during a-C deposition was investigated using a single Langmuir probe. The performance of the a-C-coated SS316L was assessed in a simulated PEMFC environment. Furthermore, in situ electrochemical impedance spectroscopy (EIS) and scanning vibrating electrode technique (SVET) were employed to monitor the evolution of electrochemical characteristics and reveal the roles of porosity and galvanic corrosion on the performance degradation. This study offers a new strategy for the large-scale application of high-performance a-C-coated metallic BPs.

2. EXPERIMENTAL DETAILS

2.1. Sample Preparation

Commercial SS316L sheets with a thickness of 0.1 mm and P-type monocrystalline silicon (100) sheets were utilized as substrates. The a-C films were fabricated through direct-current magnetron sputtering (DCMS) using a 99.99% pure graphite target (380 mm × 100 mm × 7 mm). To enhance adhesion, a Cr transition layer was deposited by high-power impulse magnetron sputtering (HiPIMS) with a 99.999% pure Cr target of the same dimensions. Prior to being placed in the chamber, the polished SS316L sheets were subjected to ultrasonic cleaning in acetone and ethanol for 15 min to eliminate surface oil and impurities. Once the vacuum reached 2×10^{-5} Torr, the substrates were etched by Ar^+ glow discharge at a bias of −500 V for 30 min to eliminate the surface oxide layer. Subsequently, the Cr transition layer was deposited by HiPIMS at a bias of −100 V for 30 min. Following this, after setting the base magnetic field, an additional external magnetic field was introduced, and its rotation angle was adjusted to achieve different magnetic field distributions. In this setup, a positive angle denotes an outward rotation of the magnetic field, as illustrated in Figure 1. The rotation angles employed in this study were −60°, −30°, 0°, 30°, 60°, and 90°. By rotating the external magnetic component, both the geometry and local intensity of the magnetic field near the target surface could be tuned without altering the overall power input, thereby enabling independent control over the magnetic field distribution and strength. The thickness of all a-C films was maintained at approximately 180 nm by regulating the deposition time.

The plasma behavior under varying magnetic field rotation angles was investigated by a single Langmuir probe system (LP-500 ALP system, Impedans Ltd.) with a 0.35 mm radius tungsten wire.[25,26] The exposed tip length of the Langmuir probe was 8.5 mm, with the remaining components enclosed in a ceramic tube. The probe was positioned 1 cm from the substrate surface. Current−voltage (I−V) characteristics were obtained by applying a swept voltage from −10 V to +15 V in the time-integration mode. The electron density (n_e) and plasma potential (V_p) were deduced from the plasma I−V characteristics, providing insight into the incident ion energy.

2.2. Characterization of a-C Films

The study utilized scanning electron microscopy (SEM, Verios G4 UC, US) to examine the thickness and cross-sectional morphology of the a-C films. Furthermore, the composition and atomic bond state were analyzed by X-ray photoelectron spectroscopy (XPS, Axis UltraDLD, JP) with monochromatic Al Kα irradiation. The C 1s spectra were fitted using Casa2273 software with a combination of Gaussian (20%) and Lorentzian (80%) functions after Shirley background subtraction, in order to calculate the content of sp^2-C and sp^3-C. No pretreatment was employed before XPS tests in order to maintain the original surface chemical state. The carbon bond structure of the a-C films was analyzed using a Raman spectrometer (Renishaw inVia Reflex, UK) with a 532 nm wavelength laser. The stretching vibration absorption peak (D-peak) at ∼1360 cm^{-1} and the respiratory vibration absorption peak (G-peak) at ∼1560 cm^{-1} are two typical characteristic peaks of a-C films.[27] The ratio of sp^2/sp^3, the diameter of sp^2 clusters, and disorder degrees were evaluated by analyzing the intensity ratio of the D-peak and G-peak (I_D/I_G), as well as the G-peak position and full width at half-maximum of the G-peak (G-fwhm).

A transmission electron microscope (TEM, Technai F20, US) with an accelerating voltage of 200 kV and a point resolution of 0.24 nm was utilized to investigate the microstructure and morphology of the films. TEM samples were prepared using focused ion beam (FIB, Auriga, GER) with a Ga ion beam. The sp^2-C fraction of the films was determined through electron energy loss spectroscopy (EELS) in TEM. This was achieved by calculating the area ratio of the π^* and σ^* states of the test samples using the double window method. Highly oriented pyrolytic graphite (HOPG) served as the reference material for these measurements.

https://doi.org/10.1021/acsami.6c03124
ACS Appl. Mater. Interfaces 2026, 18, 36164−36176

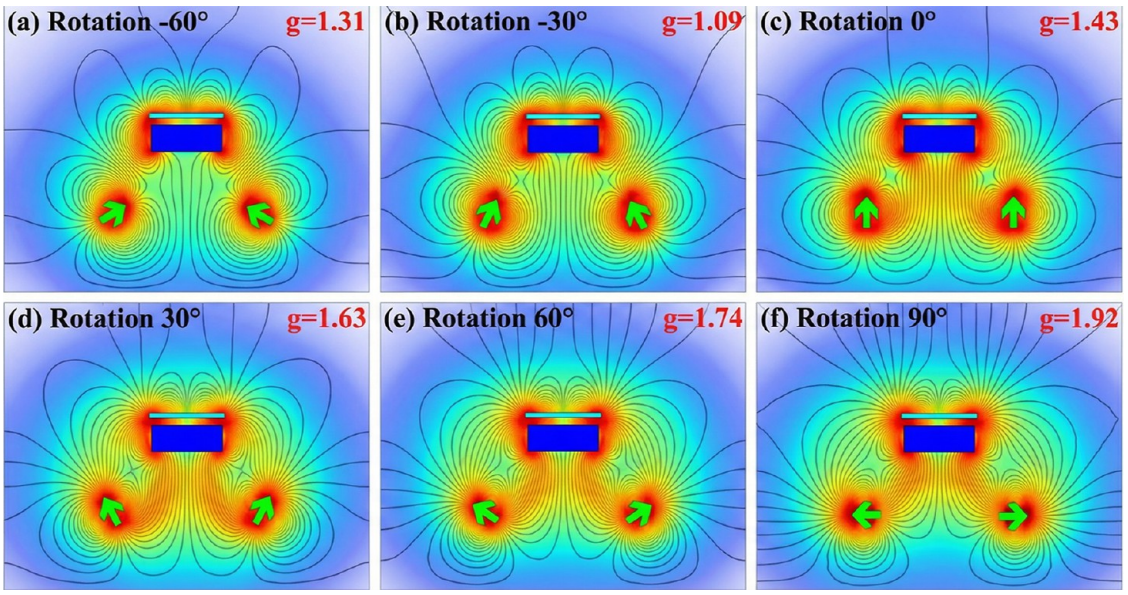

Figure 2. Schematic diagram of magnetic field line distribution intervened by a rotatable magnetic field of (a) −60°, (b) −30°, (c) 0°, (d) 30°, (e) 60°, and (f) 90°.

2.3. Electrochemical Measurements

The evaluation of the corrosion resistance of a-C coated BPs was conducted in accordance with the 2025 standard of the U.S. Department of Energy (DOE2025).[28] Electrochemical corrosion tests were carried out by a Gamry electrochemical workstation (reference 600+, US) in pH = $3H_2SO_4$ and 0.1 ppm HF at 80 °C. The three-electrode system was used, in which the sample was the working electrode, Pt was the counter electrode, and Ag/AgCl was the reference electrode. The standard electrode potential of the KCl-saturated Ag/AgCl reference electrode in this study was 0.1989 V vs standard hydrogen electrode (SHE) at 25 °C. The potentiodynamic polarization test was scanned from −0.3 to 1.2 V vs SHE at the speed of 0.1 mV/s. The anodic potentiostatic polarization test was carried out at 1.0 V vs SHE for 48 h in the solution aerated with air purge, while the cathodic potentiostatic polarization test was carried out at −0.1 V vs SHE for 48 h in the solution aerated with H_2 purge.

In situ EIS was conducted with a 10 Hz sinusoidal perturbation, within the frequency range of 100 kHz to 10 mHz, at different time intervals (2, 6, 12, 24, and 48 h) during anodic potentiostatic polarization tests.[29] The current density distribution during potentiostatic polarization at 1.0 V vs SHE was obtained using a VersaSCAN microscanning electrochemical workstation (AMETEK, USA). Simultaneously, Scanning Vibrating Electrode Technique (SVET) scans were performed at consistent time intervals over a 4 mm × 4 mm area with 31 × 31 measurement points. A microelectrode (50 μm in diameter) was vibrated perpendicular to the surface at 80 Hz with an amplitude of 30 μm. Prior to testing, the open-circuit potential (OCP) of all samples was monitored for 2 h to ensure electrochemical equilibrium in all subsequent measurements.

After the 48 h anodic potentiostatic polarization test, the corrosive solution was gathered, and the concentration of released ions in the solution was analyzed using an inductively coupled plasma emission spectrometer (ICP−OES, Spectro Arcos II, GER).

2.4. ICR Measurements

The interfacial contact resistance (ICR) was measured before and after anodic potentiostatic tests at a compaction force of 1.38 MPa. The BPs were sandwiched between two carbon papers (Toray 060) to simulate the real conditions of PEMFCs. The ICR between the coated samples and gold-coated copper plates was determined by using a DC low-resistance tester (JK2511B).

3. RESULTS AND DISCUSSION

3.1. Magnetic Field Distribution and Unbalance Coefficient

Based on the magnetic field structures, magnetrons can be categorized into balanced and unbalanced types. In magnetron sputtering discharge, the liberation of electrons from the control of the magnetic field is determined by the zero point of the magnetic field in the plasma above the surface of the target. If the zero point of the magnetic field is positioned too far from the target, the electrons are scarcely able to escape the confines of the magnetic field, which is referred to as a balanced magnetic field. Conversely, if the zero point of the magnetic field is closer to the target surface, the electrons find it easier to escape the constraints of the magnetic field, which is referred to as an unbalanced magnetic field. The balanced field has the ability to confine more high-energy electrons, thereby enhancing the plasma density, while the unbalanced magnetic field can lead to increased ion bombardment on the substrates, at the cost of energy consumption by the electrons.[20,30] In this study, the approach proposed by Window and Savvides was utilized to assess the magnetic field configurations using the unbalanced coefficient of the magnetic field (g) as follows

$$g = Z_0/W_{1/2} \tag{1}$$

where Z_0 represents the distance from the magnetic zero point above the central magnet to the target surface and $W_{1/2}$ denotes the half-width or radius of the sputtering target.[31] In this study, the $W_{1/2}$ of the rectangular target was 50 mm. Figure 2 portrays the distribution of magnetic field lines, and the unbalance coefficients at rotation angles of −60°, −30°, 0°, 30°, 60°, and 90° were 1.31, 1.09, 1.43, 1.63, 1.74, and 1.92, respectively.

With varying distributions of magnetic fields, the typical $I-V$ characteristic curves were observed, and the corresponding electron density and plasma potential were acquired. Generally, the $I-V$ characteristics can be categorized into three regions: (1) ion-current saturation region (I_{is}), (2) transition region, and (3) electron-current saturation region (I_{es}).[25,26] When the

https://doi.org/10.1021/acsami.6c03124
ACS Appl. Mater. Interfaces 2026, 18, 36164−36176

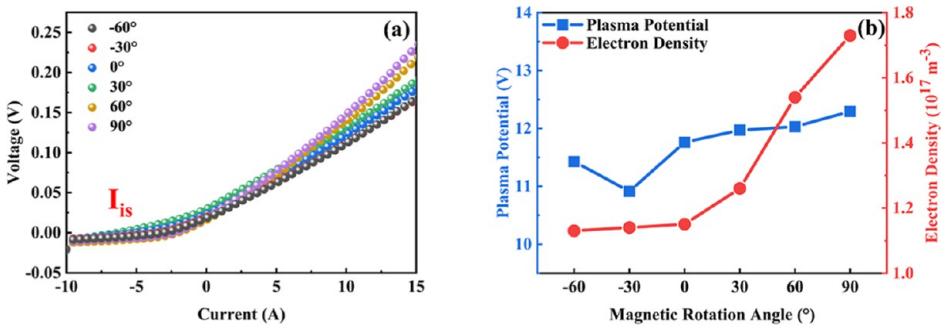

Figure 3. (a) Plasma $I-V$ characteristic curves and (b) corresponding plasma potential and electron density at different magnetic field rotation angles.

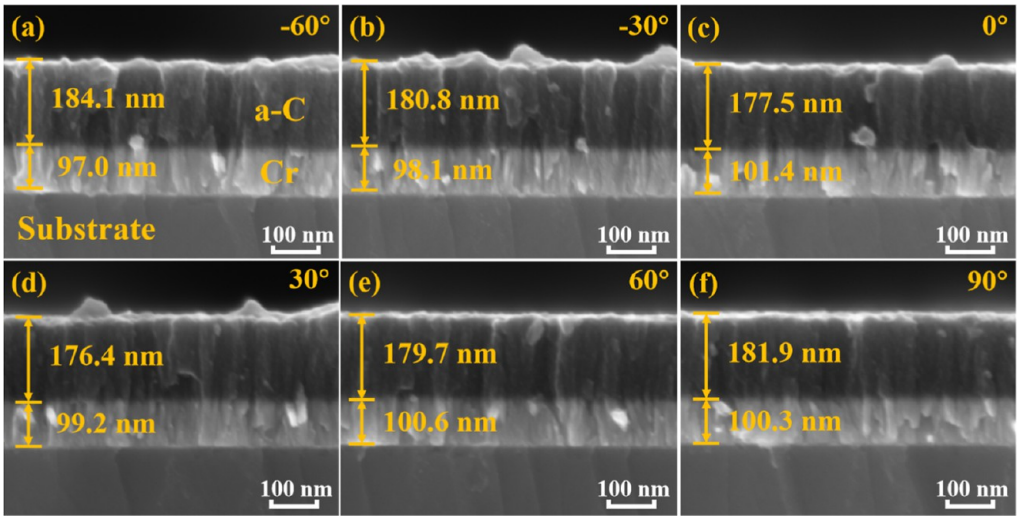

Figure 4. Cross-sectional morphology of films deposited at the magnetic field rotation angle of (a) −60°, (b) −30°, (c) 0°, (d) 30°, (e) 60°, and (f) 90°.

probe has the same potential as the plasma, the collected current primarily originates from mobile electrons. As the voltage surpasses the plasma potential, the current tends to saturate and reaches the electron-current saturation value. When the voltage is lower than the plasma potential, the electrons will be repelled, in accordance with the Boltzmann equation. As the voltage decreases to the floating potential, the probe current mainly comes from the ion current, gradually approaching the ion-current saturation value. The ion-current saturation value is much smaller than the electron-current value, given that ions have a significantly greater mass than electrons. Both the electron density and plasma potential are essential for analyzing the plasma characteristics during the deposition process, hence the focus on the transition region and I_{is}.[25,26] As the rotation angle increased from −60° to 90°, the probe current exhibited a volcanic change trend, with the maximum value appearing at −30°, as depicted in Figure 3a. Intriguingly, this trend was positively correlated with the unbalanced coefficient of the magnetic field, indicating that the electron density increased with the rise of the unbalanced coefficient of the magnetic field. The electron density (n_e) could be determined utilizing the following equation in quasi-neutral unbalanced plasma

$$n_e = \frac{1}{0.6es}\sqrt{\frac{M_i}{kT_e}}\cdot I_{is} \quad (2)$$

where e represents the charge of the electron, s denotes the area of the exposed probe surface, M_i stands for the ion mass of the gaseous ion, k is Boltzmann's constant, and I_{is} indicates the ion-current saturation value.[12] The role played by the kinetic energy of ions in determining the microstructure of a-C films was of great significance as it could be reflected by the plasma potential. As the rotation angle increased from −60° to 90°, the plasma potential decreased from 11.4 V at −60° to 10.9 V at −30° and then increased to 12.3 V at 90°. This implies that the kinetic energy of ions and the ionization degree of plasma increased slightly with the increase of the unbalanced coefficient of the magnetic field, as depicted in Figure 3b. The electron density remained stable at approximately 1.14×10^{17} m^{-3} within the balanced field range ($g \leq 1.5$) due to the strong binding ability of the balanced magnetic field to electrons, resulting in few ions reaching the substrate. With a further increase in the unbalanced coefficient of the magnetic field ($g \geq 1.5$), the magnetic lines of flux were able to penetrate the substrate more, leading to a significant increase in the electron density to 1.73×10^{17} m^{-3} at 90°. Generally, the electron density theoretically equals the ion density in plasma, indicating that the highest plasma ion density might appear at 90°.

3.2. Morphology and Characterization of Deposited Films

In order to mitigate the impact of thickness on subsequent performance evaluations, the thicknesses of a-C layers and Cr layers in all samples were maintained at 180 ± 5 nm and 100 ±

https://doi.org/10.1021/acsami.6c03124
ACS Appl. Mater. Interfaces 2026, 18, 36164−36176

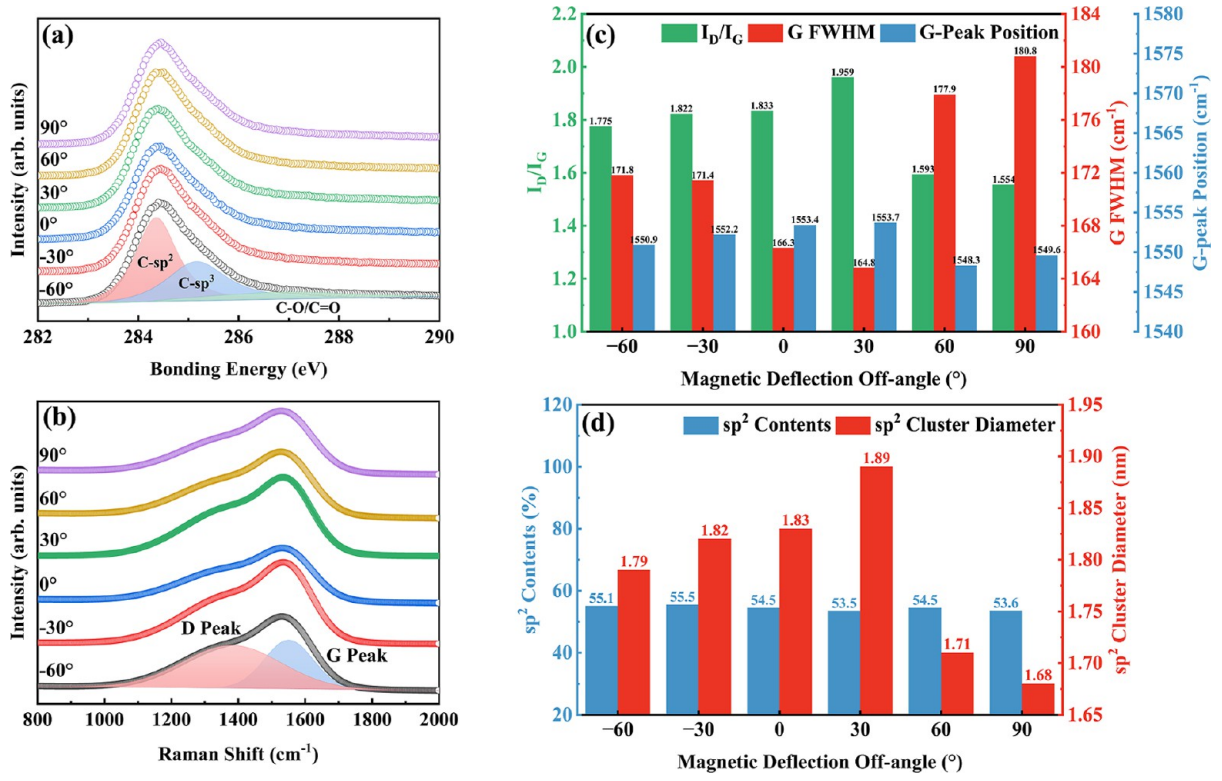

Figure 5. (a) C 1s peaks, (b) Raman spectra, (c) I_D/I_G ratio, G-peak position, and G-fwhm, and (d) corresponding diameter of sp^2 clusters of a-C films deposited at various magnetic field rotation angles.

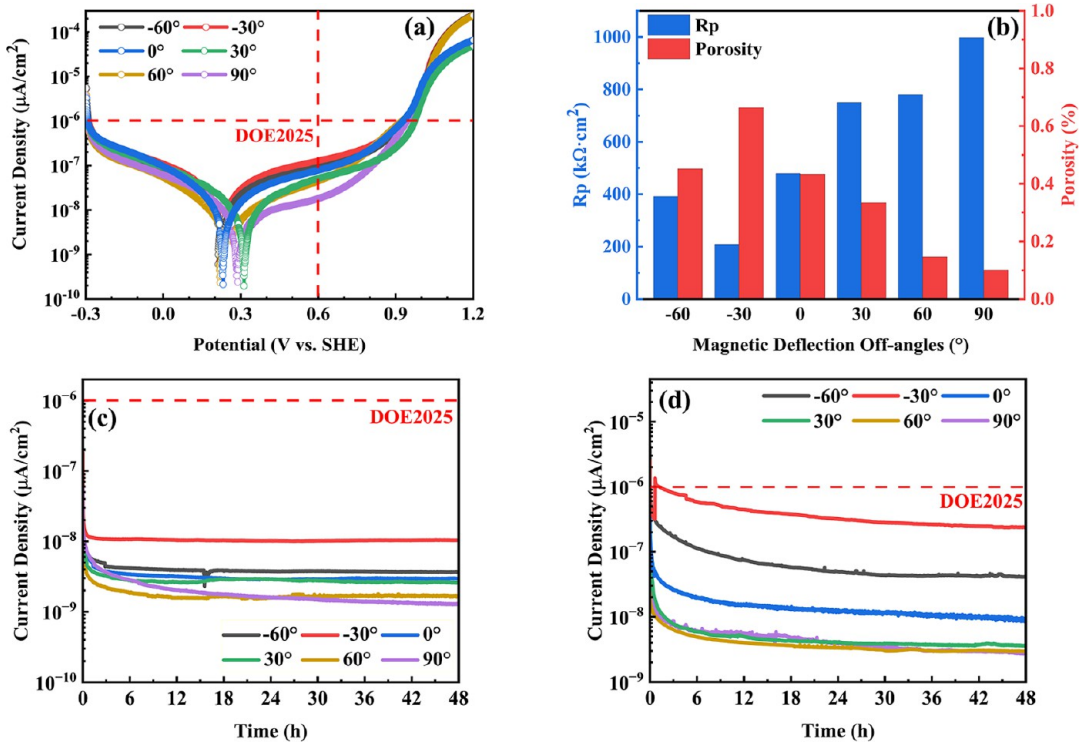

Figure 6. (a) Potentiodynamic polarization curves, (b) the calculated R_p and porosity, and (c) cathodic and (d) anodic potentiostatic tests curves of the films deposited at various magnetic field rotation angles.

3 nm, respectively, as depicted in Figure 4. Irrespective of magnetic field rotation angles, the cross-sectional morphologies of the deposited films exhibited uniformity with no discernible macro-defects. The underlying Cr transition layer displayed a distinct columnar growth trend, with no evidence of cracking or peeling at the interface.

The XPS technique was employed for the quantitative analysis of variations in carbon bonding content within a-C

https://doi.org/10.1021/acsami.6c03124
ACS Appl. Mater. Interfaces 2026, 18, 36164−36176

films deposited at various angles of magnetic field rotation. These films were primarily comprised of carbon and oxygen, with the small quantity of oxygen likely stemming from residual oxygen in the vacuum chamber during deposition and oxygen absorption from the atmosphere.[11,32,33] The proportions of sp^2-C (~284.6 eV), sp^3-C (~285.2 eV), and C−O/C = O (~286.6 eV) were determined through the fitting of C-1s spectra, as illustrated in Figure 5a.[32−35] Across different angles of magnetic field rotation, the sp^3-C and sp^2-C contents remained consistently around 34% and 55%, respectively.

The carbon bonding structure of a-C films deposited at various magnetic field rotation angles was further investigated using Raman spectroscopy. After linear background subtraction, all a-C films exhibited two characteristic Gaussian peaks: the D-peak and the G-peak, as illustrated in Figure 5b. The I_D/I_G ratio, G-peak position, and G-fwhm provide insights into the sp^2-C content, sp^2 cluster diameter, and structural disorder, as shown in Figure 5c.[36] As the magnetic field rotation angle increased, the I_D/I_G ratio increased from 1.78 at −60° to 1.96 at 30° and then declined to 1.55 at 90°, indicating that the largest sp^2 cluster diameter occurred at 30°. Conversely, the G-peak position remained unaffected by the magnetic field angle, suggesting that the sp^2-C content was stable, in agreement with XPS results. The G-fwhm decreased from 171.8 cm^{-1} at −60° to 164.8 cm^{-1} at 30° and then increased to 180.8 cm^{-1} at 90°, reflecting a decrease in structural disorder followed by an increase. Due to the diameter of the sp^2 cluster in the films being closely related to the I_D/I_G, the average cluster diameter (L_a) in the a-C films can be calculated as follows

$$I_D/I_G = C(\lambda)\cdot {L_a}^2 \tag{3}$$

where $C(\lambda)$ is the factor related to wavelength, which is C (532 nm) = ~0.55 nm^{-2} here.[30,37] As the magnetic field rotation angle increases, L_a increases from 1.80 nm at −60° to 1.89 nm at 30° and then decreases to 1.68 nm at 90° due to the dispersion or aggregation of sp^2 clusters caused by the variation of the number and energy of C ions. Compared with the XPS result, the diameter of sp^2 clusters could be effectively adjusted without influencing the contents of sp^2-C by changing the rotation angle of the magnetic field.

3.3. Electrochemical Properties and ICR

In Figure 6a, the corrosion current density of all a-C coated SS316L did not exceed 1 $\mu A/cm^2$ within the range of −0.2−0.8 V vs SHE, and there was no discernible active peak. As the rotation angle of the magnetic field increased from −60° to 90°, the free corrosion potential (E_{corr}) of all samples remained around 265 ± 50 mV, while the corrosion current density (i_{corr}) initially increased from 6.4×10^{-2} $\mu A/cm^2$ at −60° to 8.1×10^{-2} $\mu A/cm^2$ at −30° and then decreased to 2.0×10^{-2} $\mu A/cm^2$ at 90°. All curves exhibited evident passivation in the anode region, which may be attributed to the anodic dissolution of the Cr transition layer or the SS316L substrate.[38]

Hence, the assessment of the corrosion resistance of the deposited films hinged significantly on their porosity. The polarization resistance (R_p) and porosity levels can be determined by the Tafel extrapolation method to fit the potentiodynamic polarization curve

$$R_p = \frac{\beta_a\beta_c}{2.303 i_{corr}(\beta_a + \beta_c)A} \tag{4}$$

$$\text{porosity} = \left(\frac{R_{p(substrate)}}{R_{p(film)}}\right) 10^{(-|\Delta E|/\beta_a)} \tag{5}$$

where β_a and β_c represent the anodic and cathodic Tafel polarization slopes, respectively, i_{corr} denotes the corrosion current density, and A is the exposed area of the test samples, which is 1 cm^2 in this study. $R_{p(substrate)}$ and $R_{p(film)}$ signify the polarization resistances of the substrate and coated samples respectively, while $|\Delta E|$ represents the absolute value of the potential difference between the free corrosion potentials of the coated samples and the substrates.[39] As the magnetic field rotation angle increased, the R_p decreased from 391.87 kΩ·cm^2 at −60° to 208.32 kΩ·cm^2 at −30°, subsequently rising to 997.72 kΩ·cm^2 at 90°. Conversely, the porosity exhibited an opposing trend, aligning with the i_{corr} results. Consequently, we suggest that the insufficient corrosion resistance of the a-C film deposited at −30° could be attributed to its high porosity (0.66%).

In order to assess their long-term corrosion resistance, both cathodic and anodic potentiostatic polarization tests were conducted over 48 h, as illustrated in Figure 6c,d. Following the completion of the cathode and anode potentiostatic polarization tests, all specimens maintained a consistently low i_{corr} level, which satisfies the standards in DOE2025. Under cathodic potentiostatic polarization conditions, the i_{corr} values exhibited a noteworthy variation with the rotation angle of the magnetic field. Specifically, the i_{corr} increased from 3.73×10^{-3} $\mu A/cm^2$ at −60° to 1.03×10^{-2} $\mu A/cm^2$ at −30°, subsequently decreasing to 1.29×10^{-3} $\mu A/cm^2$ at 90°, as depicted in Figure 6c. Intriguingly, a similar trend was observed during the anodic potentiostatic polarization test, albeit at a higher level. The lowest i_{corr} value of 2.61×10^{-3} $\mu A/cm^2$ occurred at 90°, implying a greater susceptibility to damage under anodic polarization conditions in an oxygen-rich environment.

To authenticate the anodic dissolution of the Cr transition layer or the SS316L substrate, the corrosive solution was retrieved and examined through ICP-OES subsequent to the 48 h anodic potentiostatic test, as depicted in Table 1. The primary metallic ions identified were Fe and Cr, which happened to be the most abundant constituents in SS316L, thereby signifying the corrosion and dissolution of the substrates. As the magnetic field rotation angle increased, the concentration of metal ions initially ascended and subsequently dwindled, with both Fe and Cr reaching their pinnacle at −30°, measuring 2.84 and 1.48 ppm, respectively. This outcome was consistent with the corrosion resistance of the deposited a-C. Furthermore, it is noteworthy that the concentration of Fe greatly surpassed that of Cr, as the latter had the propensity to form the passive layer.[12,40]

Table 1. Concentrations of Fe and Cr Ions in Corrosive Solution after 48 h Anodic Potentiostatic Polarization Test

Released Metal Ions (ppm)	Magnetic Deflection Off-Angles (°)					
	−60	−30	0	30	60	90
Cr	0.52	1.48	0.19	0.05	-	-
Fe	2.68	2.84	2044	1.55	0.39	0.34

The in situ EIS tests provided an effective means to monitor the real-time corrosion process of a-C-coated SS316L in a simulated environment of PEMFCs.[12,29,40−42] Unlike passive

https://doi.org/10.1021/acsami.6c03124
ACS Appl. Mater. Interfaces 2026, 18, 36164−36176

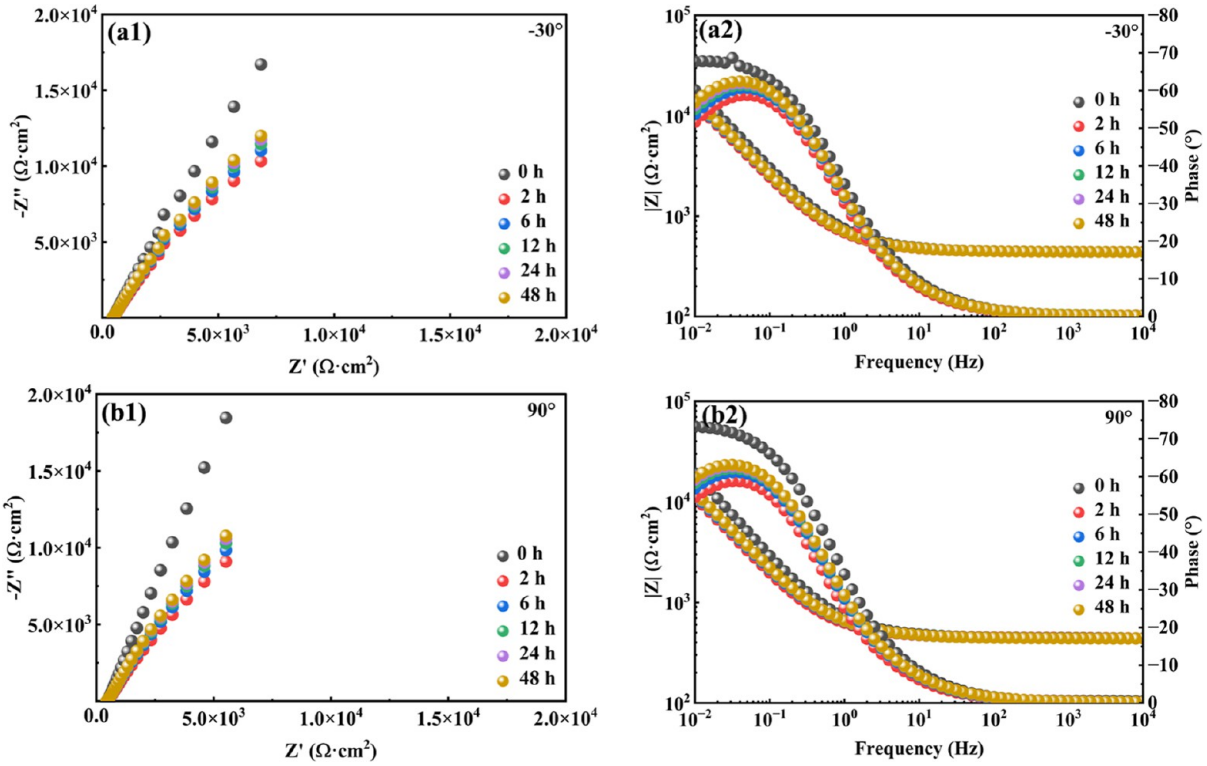

Figure 7. Nyquist and Bode impedance plots of a-C films deposited at the magnetic field rotation angle of (a) −30° (representing balanced field) and (b) 90° (representing unbalanced field).

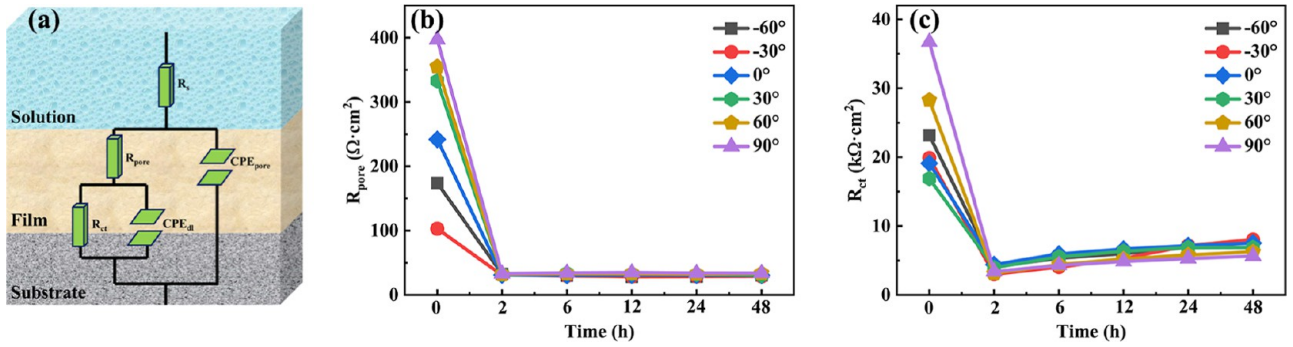

Figure 8. (a) Electronic equivalent circuits and the fitted (b) R_{pore} and (c) R_{ct}.

metals, the corrosion resistance of a-C films primarily manifested in their physical shielding effect. The in situ EIS tests were conducted on samples that had been corroded for 0, 2, 6, 12, 24, and 48 h as the corrosion reaction was initially rapid and then stabilized, as depicted in Figure 7. The capacitive loop diameter of all tested samples notably decreased during the initial stage of anodic polarization and then stabilized and slightly increased after 2 h, as evidenced by the Nyquist diagram. Likewise, the absolute impedance value at 0.01 Hz ($|Z|_{0.01}$) followed the same trend, serving as an indicator of the anticorrosion ability of the a-C films in this study, as illustrated in the Bode diagram. The low-frequency phase angle of all samples decreased significantly from approximately 75° to 60° following polarization, while the medium- and high-frequency phase angles showed no significant difference. This observation suggested that the corrosive solution continued to permeate through the defects to the substrates or chromium transition layers, gradually reinforcing the low-frequency electrode reaction.[43]

The in situ EIS data were accurately described by electronic equivalent circuits containing two time-constants, as depicted in Figure 8a. In this circuitry, R_s denotes the solution resistance, R_{pore} represents the pore resistance of a-C films, and R_{ct} signifies the charge-transfer resistance at the surface of the substrates. Recognizing the adverse impact of the coated electrode's rough surface on the scattering effect, the substitution of ideal capacitor elements with constant phase elements (CPE) was deemed necessary.[38] The impedance of CPE can be characterized as follows

$$Z_{CPE} = [Y(j\omega f)^n]^{-1} \quad (6)$$

where $j = -1^{0.5}$, $\omega = 2\pi$, f is the frequency, n and Y are the parameters of the CPE. The nearer the value of n approaches 1, the more closely CPE to an optimal capacitance. As such, CPE_{pore} represents the capacitance exhibited by the films, while CPE_{ct} denotes the capacitance associated with the dual layer at the interface connecting the electrolyte and substrate. The

https://doi.org/10.1021/acsami.6c03124
ACS Appl. Mater. Interfaces 2026, 18, 36164−36176

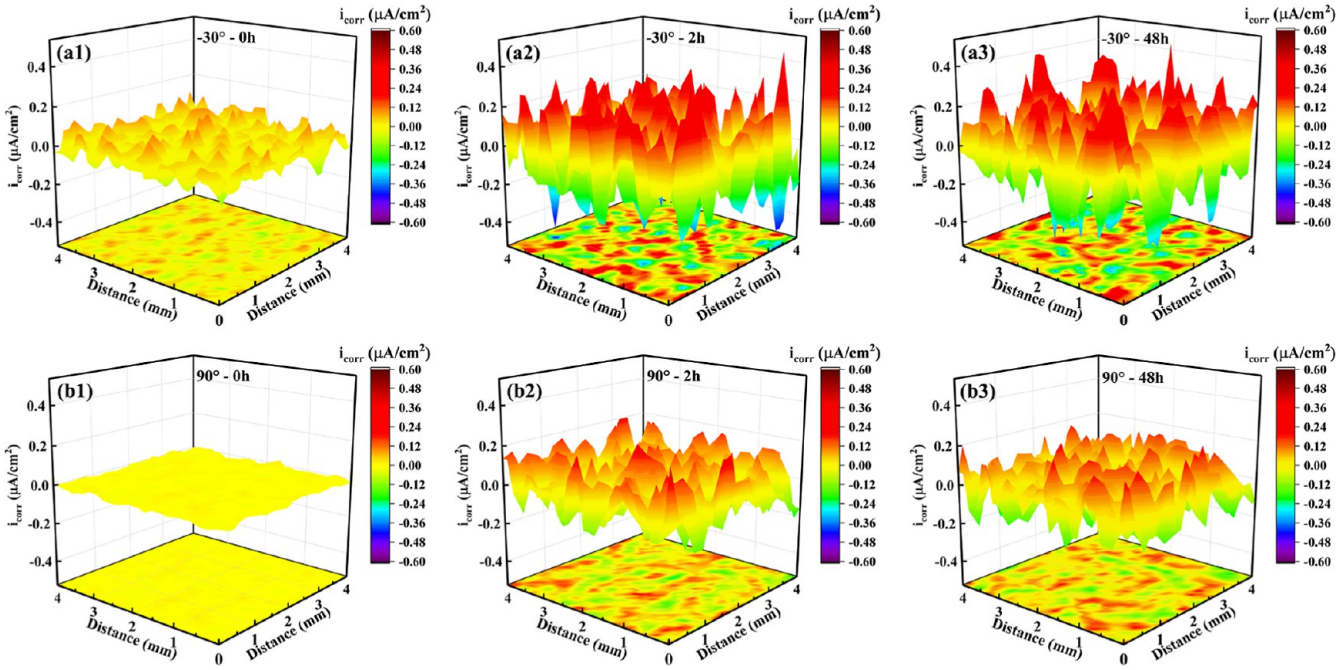

Figure 9. Current density distribution mappings of a-C films deposited at the magnetic field rotation angle of (a) −30° (representing balanced field) and (b) 90° (representing unbalanced field) for 0, 2, and 48 h.

outcomes of the fitting process can be found in the Supporting Information (Table S1, Supporting Information).

By examining the relevant parameters of the aforementioned equivalent circuit, particularly R_{pore} and R_{ct}, the mechanism behind the performance evolution of the coated samples during the process of anodic polarization can be illuminated. Prior to the polarization test, it was observed in Figure 8b that the sample at 90° exhibited the highest R_{pore} (397 Ω·cm^2), whereas the −30° sample displayed the lowest R_{pore} (103 Ω·cm^2), correlating with the porosity of the a-C films. In general, a higher R_{pore} indicates greater compactness of the deposited a-C films, thereby impeding the rapid diffusion of corrosive solutions. As the polarization test commenced, the R_{pore} of all a-C films swiftly decreased to approximately 30 Ω·cm^2, likely attributed to the rapid ion diffusion through internal defects under the influence of the applied electric field.[43]

The R_{ct} value represents the extent of the electrochemical reaction at the interface between the film and substrate. Before the polarization test, the a-C film deposited at 90° exhibited the highest R_{ct} value (36.7 kΩ·cm^2), whereas the film deposited at 30° displayed the lowest R_{ct} value (16.9 kΩ·cm^2), as illustrated in Figure 8c. It should be noted that the carrier concentration of a-C films, being a semiconductor material, played a crucial role in determining the thickness of the interfacial electric double layer and subsequently affecting the R_{ct} value.[44] Consequently, the 30° sample with a larger cluster diameter showed a lower R_{ct} value, suggesting that the increased cluster diameter resulted in higher carrier concentration and conductivity. Furthermore, the subsequent significant decrease in R_{ct} during the polarization test can be attributed to the continuous corrosion of the underlying metals.[29,44] Interestingly, after 2 h, all samples showed a gradual increase in R_{ct}. Notably, the sample with lower porosity exhibited a smaller rise in R_{ct}. For example, the R_{ct} of the 90° sample increased only from 3.39 kΩ·cm^2 at 2 h to 5.56 kΩ·cm^2 at 48 h, while that of the higher-porosity 30° sample nearly tripled, from 3.00 kΩ·cm^2 to 8.04 kΩ·cm^2, over the same period. This trend can be attributed to the formation of corrosion products at the interface, which contributed to its long-term corrosion resistance.[40,45]

The double-layer capacitance CPE_{dl} indirectly reflects the extent of the substrate corrosion reaction. Given the conductive nature of stainless steel, CPE_{dl} is primarily governed by the capacitance of the passive film.[46] It can be expressed as

$$CPE_{dl} = \frac{\gamma \varepsilon_0 \varepsilon_{dl} A_s P}{d_p} \tag{7}$$

where γ is the surface roughness factor, ε_0 is the permittivity of free space (8.845×10^{-12} F/m), ε_{dl} is the dielectric constant of the passive film, P is the coating porosity, A_s is the exposed substrate area, and d_p is the passive film thickness. After long-term corrosion, all samples exhibited a significant decrease in CPE_{dl} (Table S2), suggesting that the passive film thickened over time and eventually stabilized.

The SVET tests were conducted at time intervals of 0, 2, 6, 12, 24, and 48 h during anodic potentiostatic polarization in order to observe the in situ electrochemical activity of the a-C films.[47] As the electrochemical activity remained consistent from 2 to 48 h, the typical SVET test data for 0, 2, and 48 h are presented in Figure 9. Furthermore, the potential values obtained from SVET tests can be converted into i_{corr} for analysis using the following equation

$$i_{corr} = -\Delta\phi \frac{k}{d} \tag{8}$$

where $\Delta\phi$ is the electric potential drop, k is the electrolyte conductivity, and d is the vibration amplitude.[48,49]

The electrochemical activity of all the a-C films exhibited a rapid increase upon anodic polarization while remaining stable throughout the polarization process, thereby consistent with the findings of the potentiostatic polarization test. However, in contrast to conventional polarization tests, SVET effectively

https://doi.org/10.1021/acsami.6c03124
ACS Appl. Mater. Interfaces 2026, 18, 36164−36176

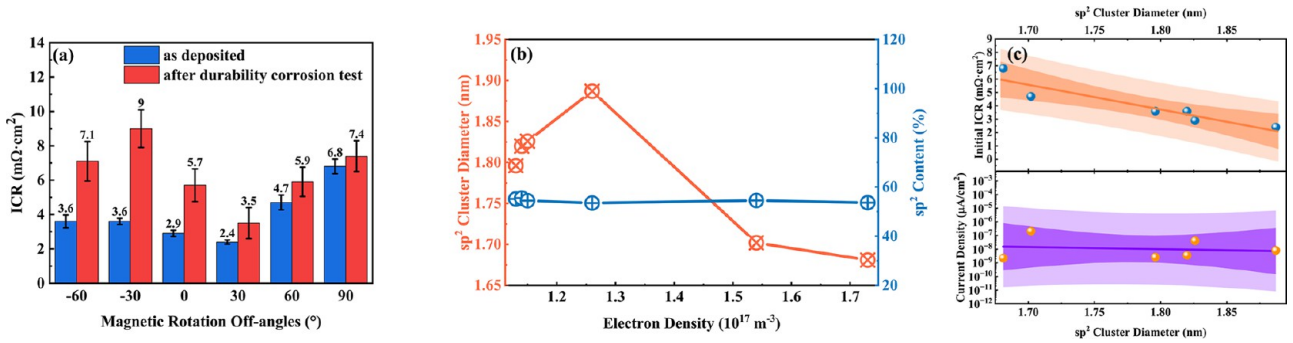

Figure 10. (a) ICR values of films deposited at various magnetic field rotation angles, before and after the corrosion durability test, (b) diameter and content of sp^2 clusters in a-C films deposited at different magnetic field rotation angles, and (c) initial ICR and current density show a linear relationship with the diameter of sp^2 clusters.

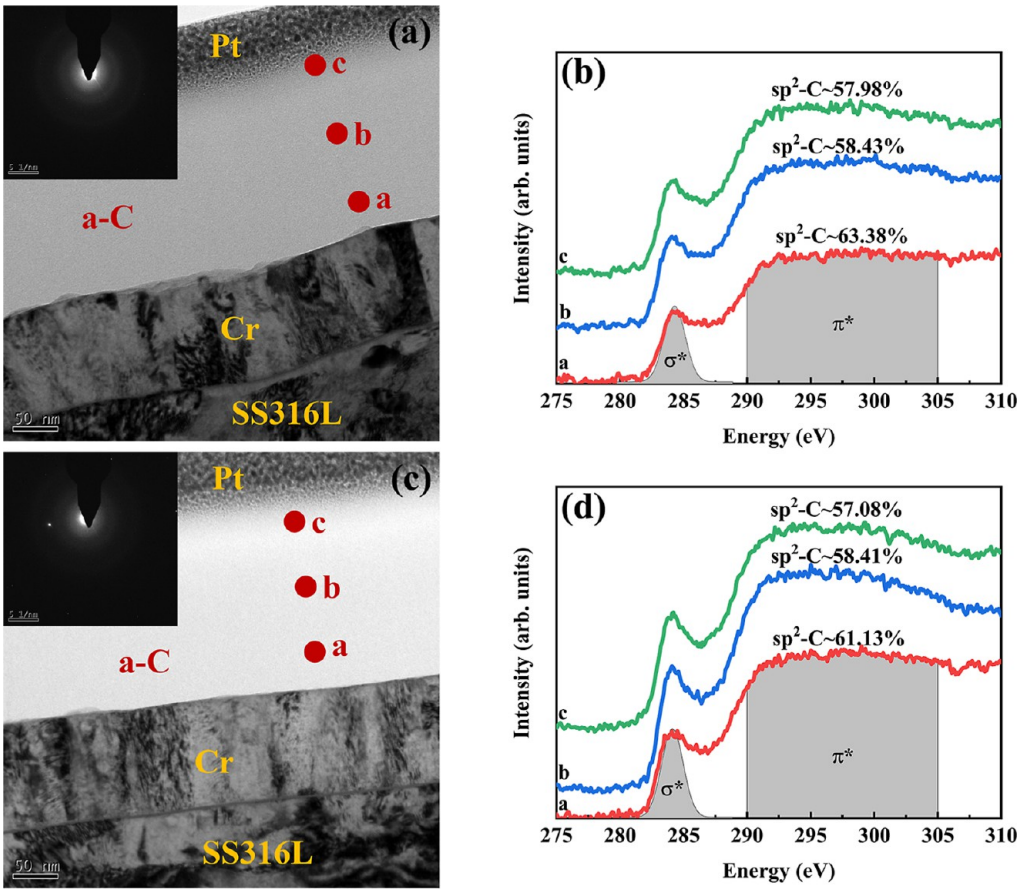

Figure 11. Cross-sectional TEM image and corresponding SAED and EELS spectra obtained from different points labeled a−c (a,b) before and (c,d) after the potentiostatic test.

discerned the disparities in local electrochemical activity. Notably, after 48 h of anodic polarization test, the average i_{corr} of the −30° sample amounted to approximately 8.33×10^{-2} $\mu A/cm^2$, yet the localized i_{corr} soared as high as ~0.53 $\mu A/cm^2$, as illustrated in Figure 9b. These sites exhibiting localized high i_{corr} will become critical locations for corrosion initiation. In contrast, the average i_{corr} results obtained through conventional electrochemical corrosion testing may mislead researchers into believing that the film retains superior corrosion resistance until the occurrence of its catastrophic failure. Furthermore, the samples possessing a larger sp^2 cluster diameter (−60°, −30°, 0°, and 30°) exhibited significantly elevated levels of localized i_{corr} compared to the other samples (60° and 90°). Evidently, this observation indicated that the enhanced conductivity resulting from larger sp^2 clusters would exacerbate galvanic corrosion during polarization, eventually leading to the deterioration of their long-term performance.

The ICR is a crucial standard for assessing the properties and longevity of BPs. Consequently, the ICR was measured before and after anodic corrosion, as illustrated in Figure 10a. Before polarization tests, the initial ICR of the coating showed a significant correlation with sp^2 cluster diameter (Figure 10c). In contrast, the diameter of sp^2 clusters did not exhibit a significant effect on corrosion current density, which appears to be more closely associated with coating porosity (Figure 4b). Specifically, larger sp^2 cluster diameters corresponded to lower

https://doi.org/10.1021/acsami.6c03124
ACS Appl. Mater. Interfaces 2026, 18, 36164−36176

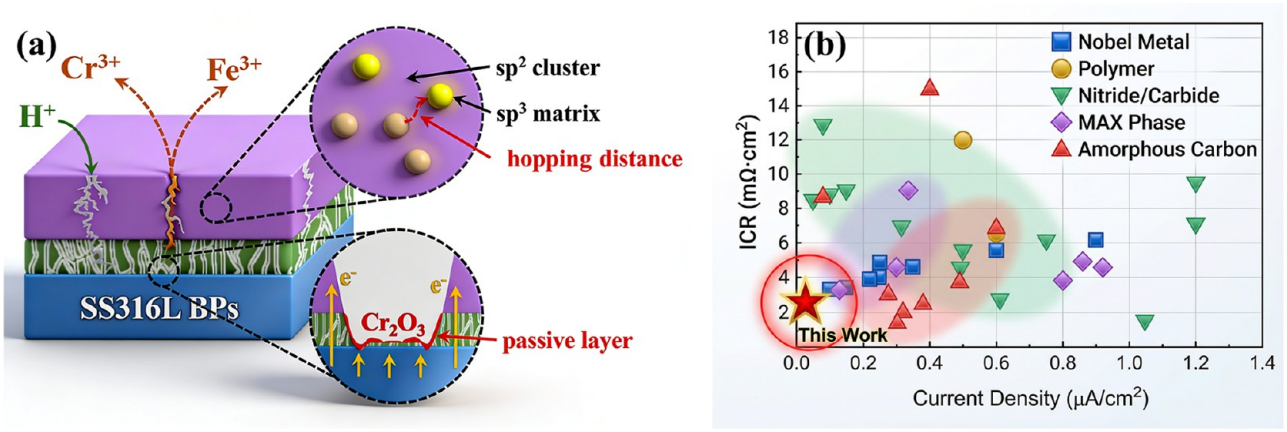

Figure 12. (a) Schematic diagram of the carrier transport and corrosion failure mechanism of a-C films and (b) performance diagram of representative films and a-C films in this work.

initial ICR values, with the minimum value of 2.4 mΩ·cm^2 observed in the sample deposited at 30°. After polarization tests, although all ICR values increased significantly, they still complied with the DOE2025 standard. The ICR of the −30° sample peaked at 9.0 mΩ·cm^2, attributable to its highest porosity and the resultant abundant corrosion products at the interface postcorrosion.[12] Conversely, the 90° sample demonstrated the smallest ICR increase, from 6.8 mΩ·cm^2 to 7.4 mΩ·cm^2, due to its superior compactness and high resistance to galvanic corrosion. The a-C film prepared at 30° exhibited the lowest ICR of 3.5 mΩ·cm^2 after 48 h of corrosion owing to its initially lowest ICR and good corrosion resistance.

3.4. Microstructural Characterization after the Potentiostatic Tests

To examine the microstructure of a-C films, the −30° sample with the most severe damage was chosen. In Figure 11, the a-C films exhibited a consistent and dense amorphous structure before and after corrosion, with selected area electron diffraction (SAED) only showing a diffuse halo. Using EELS, the internal composition of the a-C films before and after corrosion can be analyzed, as illustrated in Figure 11b,d. The proportion of sp^2-C (x) was determined using the double window method, as follows

$$\frac{(S\pi^*/S\sigma^*)_{\text{film}}}{(S\pi^*/S\sigma^*)_{\text{standard}}} = \frac{3-x}{4x} \quad (9)$$

where Sπ* and Sσ* represent the π* and σ* peak integral areas, as delineated by the gray regions in Figure 11b,d, respectively.[40,47,50,51] EELS fitting results indicated that the carbon bond structure of a-C, detected at locations a, b, and c, remained stable before and after the corrosion test.

3.5. Discussion

The magnetic field was a crucial factor influencing plasma energy and distribution during film deposition, and the composition and structure of a-C films can be precisely tailored by a rotatable magnetic field under varying unbalanced coefficients.[20,30] In this study, under a balanced magnetic field ($g \leq 1.5$), the electron density remained stable throughout the deposition process with increasing magnetic field rotation angle. However, as the unbalance coefficient increased further ($g \geq 1.5$), the electron density rose sharply, indicating a higher ionization rate.[12] This implies that more ions reached the substrate surface during unbalanced magnetron sputtering, which in turn hindered the continuous growth of sp^2 clusters, as illustrated in Figure 10b.[52] Consequently, as the rotation angle of the magnetic field ranged from −60° to 90°, the sp^2-C and sp^3-C contents of all a-C films remained stable. Nevertheless, the sp^2 cluster diameter initially increased to 1.89 nm at 30° before decreasing, resulting in the minimum initial ICR of 2.4 mΩ·cm^2.

During the protracted service of metallic BPs, the damage inflicted by corrosion proved particularly severe, closely tied to the compactness of the a-C film, as confirmed by XPS and EELS analyses of a-C films before and after potentiostatic polarization testing in simulated PEMFC environments.[12,29,40] An increase in the unbalanced coefficient of the magnetic field facilitated a rise in ion energy, resulting in a denser structure of the a-C films.[15] During the corrosion test, the −30° sample exhibited the poorest corrosion resistance due to its highest porosity, and its ICR also increased significantly, attributed to exacerbated local galvanic corrosion and the accumulation of corrosion products, as corroborated by in situ EIS tests and metal ion concentrations.[40,53,54] Specifically, employing an in situ EIS technique, it was confirmed that at the initial stage of corrosion under applied potential, the overall impedance of a-C-coated BPs decreased rapidly but soon entered a plateau stage. At this stage, both R_{pore} and R_{ct} tended to stabilize and even increased, indicating that a metal passivation film was formed at the interface, which gradually reached a dynamic equilibrium and thus inhibited further corrosion. However, the high porosity of the −30° sample hindered the stable formation of such a passivation film, leading to persistent corrosion and a marked increase in ICR. Consequently, samples with poorer corrosion resistance exhibited a more pronounced increase in ICR following long-term polarization testing.

In situ SVET measurements further confirmed that corrosion occurs in the form of local initiation (i.e., localized pitting). Compared with the average i_{corr}, the local peak i_{corr} is a better indicator of the coating's corrosion resistance. Importantly, the conductivity near defects exacerbates galvanic corrosion, which explains why films exhibiting high electrical conductivity experience more severe localized galvanic corrosion under these conditions. Therefore, reducing defects while regulating the sp^2-C clusters to shorten the carrier hopping distance and form conductive pathways, compared to simply changing the sp^2/sp^3 content, is more conducive to achieving the synergistic improvement of conductivity and

https://doi.org/10.1021/acsami.6c03124
ACS Appl. Mater. Interfaces 2026, 18, 36164−36176

corrosion resistance. This underscores the critical importance of independently controlling the microstructural architecture of a-C films, specifically the diameter of sp^2-C clusters.

In summary, the unbalanced magnetic field coefficient has the capability to alter the composition and characteristics of the a-C films by controlling the energy and distribution of plasma. While a balanced magnetic field facilitated the deposition of highly conductive a-C films with increased defect density, an unbalanced magnetic field proved to be effective in producing a-C films with superior corrosion resistance and lower initial ICR, as shown in Figure 12b. Notably, the a-C film deposited under a low unbalanced magnetic field (g = 1.63) achieved the lowest initial ICR along with excellent corrosion resistance, demonstrating the most promising potential for practical applications.

4. CONCLUSION

In this study, a range of magnetically rotated angles were employed to prepare a series of a-C-coated metallic BPs. Through the utilization of plasma diagnostics and in situ electrochemical characterization techniques, the interplay between the plasma state under diverse magnetic fields, the microstructure, and the real-time corrosion process of a-C in the PEMFCs environment was investigated. The obtained results unveiled the following findings:

(1) Adjusting the unbalanced coefficient altered the diameter of sp^2 clusters without changing sp^2 content; the a-C film deposited under a low unbalanced magnetic field (30°) exhibited the largest sp^2 cluster diameter (1.89 nm) and lowest interfacial contact resistance (ICR) before and after corrosion. This arises from increased influx of high-energy ions during magnetron sputtering, yielding denser films with enhanced corrosion resistance.

(2) In situ EIS revealed that initial corrosion under applied potential caused rapid decreases in overall impedance of a-C-coated BPs, followed by a plateau where R_{pore} and R_{ct} stabilized or increased. This indicates the formation of a metal passivation film at the interface, which reaches dynamic equilibrium to inhibit further corrosion.

(3) In situ SVET confirmed localized corrosion initiation, with local peak i_{corr} being a better indicator of coating corrosion resistance than average i_{corr}. Importantly, conductivity near defects exacerbates galvanic corrosion of the metal substrate. Thus, concurrently reducing defect density while regulating the sp^2-C clusters in a-C synergistically improves the conductivity and corrosion resistance.

■ ASSOCIATED CONTENT

Supporting Information

The Supporting Information is available free of charge at https://pubs.acs.org/doi/10.1021/acsami.6c03124.

Summary of corrosion test data and performance advantages (PDF)

■ AUTHOR INFORMATION

Corresponding Authors

Peng Guo − *State Key Laboratory of Advanced Marine Materials, Zhejiang Key Laboratory of Extreme-environmental Material Surfaces and Interfaces, Ningbo Institute of Materials Technology and Engineering, Chinese Academy of Sciences, 315201 Ningbo, PR China; Center of Materials Science and Optoelectronics Engineering, University of Chinese Academy of Sciences, 100049 Beijing, PR China*; Email: guopeng@nimte.ac.cn

Aiying Wang − *State Key Laboratory of Advanced Marine Materials, Zhejiang Key Laboratory of Extreme-environmental Material Surfaces and Interfaces, Ningbo Institute of Materials Technology and Engineering, Chinese Academy of Sciences, 315201 Ningbo, PR China; Center of Materials Science and Optoelectronics Engineering, University of Chinese Academy of Sciences, 100049 Beijing, PR China*; orcid.org/0000-0003-2938-5437; Email: aywang@nimte.ac.cn

Authors

Hao Li − *State Key Laboratory of Advanced Marine Materials, Zhejiang Key Laboratory of Extreme-environmental Material Surfaces and Interfaces, Ningbo Institute of Materials Technology and Engineering, Chinese Academy of Sciences, 315201 Ningbo, PR China*; orcid.org/0000-0001-9650-7057

Jingyun Feng − *State Key Laboratory of Advanced Marine Materials, Zhejiang Key Laboratory of Extreme-environmental Material Surfaces and Interfaces, Ningbo Institute of Materials Technology and Engineering, Chinese Academy of Sciences, 315201 Ningbo, PR China; Center of Materials Science and Optoelectronics Engineering, University of Chinese Academy of Sciences, 100049 Beijing, PR China*

Keiji Komatsu − *Graduate School of Engineering, Nagaoka University of Technology, 940-2188 Nagaoka, Japan*; orcid.org/0000-0002-1450-5064

Rende Chen − *State Key Laboratory of Advanced Marine Materials, Zhejiang Key Laboratory of Extreme-environmental Material Surfaces and Interfaces, Ningbo Institute of Materials Technology and Engineering, Chinese Academy of Sciences, 315201 Ningbo, PR China*

Guanshui Ma − *State Key Laboratory of Advanced Marine Materials, Zhejiang Key Laboratory of Extreme-environmental Material Surfaces and Interfaces, Ningbo Institute of Materials Technology and Engineering, Chinese Academy of Sciences, 315201 Ningbo, PR China; Center of Materials Science and Optoelectronics Engineering, University of Chinese Academy of Sciences, 100049 Beijing, PR China*

Hidetoshi Saito − *State Key Laboratory of Advanced Marine Materials, Zhejiang Key Laboratory of Extreme-environmental Material Surfaces and Interfaces, Ningbo Institute of Materials Technology and Engineering, Chinese Academy of Sciences, 315201 Ningbo, PR China; Graduate School of Engineering, Nagaoka University of Technology, 940-2188 Nagaoka, Japan*

Complete contact information is available at: https://pubs.acs.org/10.1021/acsami.6c03124

Notes

The authors declare no competing financial interest.

■ ACKNOWLEDGMENTS

This work was financially supported by the National Natural Science Foundation of China (52471105, U24A2030), Zhejiang Lingyan Research and Development Program (2024C01159), Zhejiang Provincial Natural Science Founda-

tion (LQN25E010007), and Natural Science Foundation of Ningbo (2025Z231, 2025QL023).

REFERENCES

(1) Kassa, T. S.; Yessuf, A. M.; Mohideen, M. M.; Mihiretu, A. M.; Ramakrishna, S.; Liu, Y. Modification, Degradation, and Mitigation of Perfluorosulfonic Acid Proton Exchange Membranes for Fuel Cells: A Review. *ACS Appl. Mater. Interfaces* **2025**, *17* (32), 45271−45301.
(2) Javed, A.; Palafox Gonzalez, P.; Thangadurai, V. A Critical Review of Electrolytes for Advanced Low- and High-Temperature Polymer Electrolyte Membrane Fuel Cells. *ACS Appl. Mater. Interfaces* **2023**, *15* (25), 29674−29699.
(3) Hu, Q.; Zhang, D.; Fu, H. Effect of flow-field dimensions on the formability of Fe−Ni−Cr alloy as bipolar plate for PEM (proton exchange membrane) fuel cell. *Energy* **2015**, *83*, 156−163.
(4) Ji, Y. Y.; Pan, C. C.; Wang, M. Y.; Behnamian, Y.; Zhao, D. D.; Hu, W. B.; Xia, D. H.; Tribollet, B. Unraveling the role of tensile stress in corrosion and the formation of oxide films on sensitized Al-Mg alloys. *Corros. Sci.* **2025**, *257*, 113306.
(5) Yi, P. Y.; Li, X. B.; Yao, L.; Fan, F.; Peng, L. F.; Lai, X. M. A lifetime prediction model for coated metallic bipolar plates in proton exchange membrane fuel cells. *Energy Convers. Manage.* **2019**, *183*, 65−72.
(6) Jia, Q.; Mu, Z.; Zhang, X.; Zhang, B.; Liu, R.; Gao, K.; Yu, Y.; Lai, Z.; Zhang, J. Electronic conductive and corrosion mechanisms of dual nanostructure CuCr-doped hydrogenated carbon films for SS316L bipolar plates. *Mater. Today Chem.* **2021**, *21*, 100521.
(7) Mani, S. P.; Agilan, P.; Kalaiarasan, M.; Ravichandran, K.; Rajendran, N.; Meng, Y. Effect of multilayer CrN/CrAlN coating on the corrosion and contact resistance behavior of 316L SS bipolar plate for high temperature proton exchange membrane fuel cell. *J. Mater. Sci. Technol.* **2022**, *97*, 134−146.
(8) Zhang, J. Y.; Zhang, Y.; Wang, Z. Y.; Ma, G. S.; Zhang, A. F.; Lee, K. R.; Wang, A. Y. Enhancing corrosion resistance of Ti2AlC MAX phase through Sn solid solution in harsh acidic environments. *Corros. Sci.* **2025**, *255*, 113073.
(9) Wu, Z.; Zhu, Q.; Ai, Z.; Bu, Q.; Ma, R.; Zhang, Z.; Xu, C.; Huan, X.; Zhang, Q. Tailored Interfacial sp(2)/sp(3) Hybridization in Diamond@DLC Heterostructure: Resolving the Microwave Absorption-Dielectric-Thermal Trilemma in Epoxy Composites for Electronic Packaging. *ACS Appl. Mater. Interfaces* **2025**, *17* (47), 64853−64863.
(10) Wang, Y.; Ruiz Diaz, D. F.; Chen, K. S.; Wang, Z.; Adroher, X. C. Materials, technological status, and fundamentals of PEM fuel cells − A review. *Mater. Today* **2020**, *32*, 178−203.
(11) Li, H.; Guo, P.; Zhang, D.; Chen, R. D.; Zuo, X.; Ke, P. L.; Saito, H.; Wang, A. Y. Influence of deposition temperature on the structure, optical and electrical properties of a-C films by DCMS. *Appl. Surf. Sci.* **2020**, *503*, 144310.
(12) Li, H.; Xin, Y.; Komatsu, K.; Guo, P.; Ma, G.; Ke, P.; Lee, K.-R.; Saito, H.; Wang, A. Controlling the compactness and sp2 clusters to reduce interfacial damage of amorphous carbon/316L bipolar plates in PEMFCs. *Int. J. Hydrogen Energy* **2022**, *47*, 11622.
(13) Li, H.; Guo, P.; Komatsu, K.; Ma, G. S.; Chen, R. D.; Ke, P. L.; Saito, H.; Wang, A. Y. Deposition temperature controlled interfacial degradation of a-C/Cr coatings for 316Lss bipolar plates in PEMFCs. *Int. J. Hydrogen Energy* **2024**, *91*, 765−774.
(14) Zuo, X.; Zhang, D.; Chen, R. D.; Ke, P. L.; Oden, M.; Wang, A. Y. Spectroscopic investigation on the near-substrate plasma characteristics of chromium HiPIMS in low density discharge mode. *Plasma Sources Sci. T* **2020**, *29* (1), 015013.
(15) Zuo, X.; Chen, R. D.; Ke, P. L.; Wang, A. Y. Gas Breakdown and Discharge Formation in High-Power Impulse Magnetron Sputtering. *IEEE Trans. Plasma Sci.* **2019**, *47* (2), 1215−1222.
(16) Zuo, X.; Chen, R. D.; Zhang, D.; Ke, P. L.; Wang, A. Y. Movement of luminous group spots on target and size modification of micro particles during cathodic vacuum arc deposition. *Vacuum* **2019**, *164*, 381−389.
(17) Zuo, X.; Chen, R. D.; Liu, J. Z.; Ke, P. L.; Wang, A. Y. The influence of superimposed DC current on electrical and spectroscopic characteristics of HiPIMS discharge. *AIP Adv.* **2018**, *8* (1), 015132.
(18) Zuo, X.; Ke, P. L.; Chen, R. D.; Li, X. W.; Oden, M.; Wang, A. Y. Discharge state transition and cathode fall thickness evolution during chromium HiPIMS discharge. *Phys. Plasmas* **2017**, *24* (8), 083507.
(19) Zuo, X.; Xia, F.; Zhang, D.; Ke, P. L.; Wang, Q. M.; Wang, A. Y. The effect of substrate bias on the characteristics of CrN coatings deposited by DC-superimposed HiPIMS system. *Int. J. Mod. Phys. B* **2017**, *31* (16−19), 1744032.
(20) Ryu, J.-T.; Honda, S.-I.; Katayama, M.; Oura, K. Field electron emission from amorphous carbon thin films grown by RF magnetron sputtering. *Curr. Appl. Phys.* **2005**, *5* (4), 387−391.
(21) Kalinnikov, G. V.; Andrievski, R. A.; Egorov, V. K. Amorphous/Nanocrystalline Films Prepared by Magnetron Sputtering with Additional External Magnetic Field. *J. Nano Res.* **2009**, *6*, 89−98.
(22) Wong, M. S.; Sproul, W. D.; Rohde, S. L. Modeling Magnetic-Fields of Magnetron Sputtering Systems. *Surf. Coat. Technol.* **1991**, *49* (1−3), 121−126.
(23) Li, H.; Guo, P.; Zhang, D.; Liu, L. L.; Wang, Z. Y.; Ma, G. S.; Xin, Y.; Ke, P. L.; Saito, H.; Wang, A. Y. Interface-induced degradation of amorphous carbon films/stainless steel bipolar plates in proton exchange membrane fuel cells. *J. Power Sources* **2020**, *469*, 228269.
(24) Zhang, F. T.; Liu, Z.; Pan, C. C.; Deng, Y. D.; Xia, D. H.; Tribollet, B. Effect of Si network continuity on the localized corrosion of AlSi10Mg alloy fabricated by selective laser melting. *Corros. Sci.* **2025**, *257*, 113336.
(25) Ryan, P. J.; Bradley, J. W.; Bowden, M. D. Comparison of Langmuir probe and laser Thomson scattering for electron property measurements in magnetron discharges. *Phys. Plasmas* **2019**, *26* (7), 073515.
(26) Britun, N.; Minea, T.; Konstantinidis, S.; Snyders, R. Plasma diagnostics for understanding the plasma−surface interaction in HiPIMS discharges: a review. *J. Phys. D: Appl. Phys.* **2014**, *47* (22), 224001.
(27) Li, H. X.; Xu, T.; Chen, J. M.; Zhou, H. D.; Liu, H. W. The effect of applied dc bias voltage on the properties of a-C:H films prepared in a dual dc−rf plasma system. *Appl. Surf. Sci.* **2004**, *227* (1−4), 364−372.
(28) Kumar, A.; Ricketts, M.; Hirano, S. Ex situ evaluation of nanometer range gold coating on stainless steel substrate for automotive polymer electrolyte membrane fuel cell bipolar plate. *J. Power Sources* **2010**, *195* (5), 1401−1407.
(29) Liu, Y.; Du, H.; Zuo, X.; Guo, P.; Liu, L.; Lee, K.-R.; Wang, A.; Ke, P. Cr/GLC multilayered coating in simulated deep-sea environment: Corrosion behavior and growth defect evolution. *Corros. Sci.* **2021**, *188*, 109528.
(30) Ferrari, A. C.; Robertson, J. Interpretation of Raman spectra of disordered and amorphous carbon. *Phys. Rev. B:Condens. Matter Mater. Phys.* **2000**, *61* (20), 14095−14107.
(31) Thornton, J. A. The Microstructure of Sputter-Deposited Coatings. *J. Vac. Sci. Technol. A-Vac. Surf. Films* **1986**, *4* (6), 3059−3065.
(32) Guo, P.; Li, X. W.; Sun, L. L.; Chen, R. D.; Ke, P. L.; Wang, A. Y. Stress reduction mechanism of diamond-like carbon films incorporated with different Cu contents. *Thin Solid Films* **2017**, *640*, 45−51.
(33) Nakao, S.; Yukimura, K.; Nakano, S.; Ogiso, H. DLC Coating by HiPIMS: The Influence of Substrate Bias Voltage. *IEEE Trans. Plasma Sci.* **2013**, *41* (8), 1819−1829.
(34) Mohagheghpour, E.; Rajabi, M.; Gholamipour, R.; Larijani, M. M.; Sheibani, S. Correlation study of structural, optical and electrical properties of amorphous carbon thin films prepared by ion beam sputtering deposition technique. *Appl. Surf. Sci.* **2016**, *360*, 52−58.
(35) Merel, P.; Tabbal, M.; Chaker, M.; Moisa, S.; Margot, J. Direct evaluation of the sp(3) content in diamond-like-carbon films by XPS. *Appl. Surf. Sci.* **1998**, *136* (1−2), 105−110.

https://doi.org/10.1021/acsami.6c03124
ACS Appl. Mater. Interfaces 2026, 18, 36164−36176

(36) Chu, P. K.; Li, L. H. Characterization of amorphous and nanocrystalline carbon films. *Mater. Chem. Phys.* **2006**, *96* (2−3), 253−277.
(37) Tuinstra, F.; Koenig, J. L. Raman Spectrum of Graphite. *J. Chem. Phys.* **1970**, *53* (3), 1126−1130.
(38) Liu, C.; Bi, Q.; Leyland, A.; Matthews, A. An electrochemical impedance spectroscopy study of the corrosion behaviour of PVD coated steels in 0.5 N NaCl aqueous solution: Part II. EIS interpretation of corrosion behaviour. *Corros. Sci.* **2003**, *45* (6), 1257−1273.
(39) Liu, Y.; Li, S.; Li, H.; Ma, G.; Sun, L.; Guo, P.; Ke, P.; Lee, K.-R.; Wang, A. Controllable defect engineering to enhance the corrosion resistance of Cr/GLC multilayered coating for deep-sea applications. *Corros. Sci.* **2022**, *199*, 110175.
(40) Li, H.; Guo, P.; Zhang, D.; Liu, L. L.; Wang, Z. Y.; Ma, G. S.; Xin, Y.; Ke, P. L.; Saito, H.; Wang, A. Y. Interface-induced degradation of amorphous carbon films/stainless steel bipolar plates in proton exchange membrane fuel cells. *J. Power Sources* **2020**, *469*, 228269.
(41) Liu, Z.; Wang, J. R.; Qin, Z. B.; Xia, D. H.; Behnamian, Y.; Hu, W. B.; Tribollet, B. A mechanistic study on stress corrosion cracking of sensitized AA5083 in a simulated water level fluctuation zone: Combined impedance analysis and tensile tests. *Corros. Sci.* **2025**, *245*, 112701.
(42) Wang, M. Y.; Ji, Y. Y.; Macdonald, D. D.; Hu, W. B.; Xia, D. H.; Tribollet, B. Microstructure-Tuned Hydrogen Embrittlement in 7050 Aluminum Alloy: Combined Impedance Analysis and Advanced Characterization. *J. Electrochem. Soc.* **2025**, *172* (9), 091502.
(43) Wang, Z. M.; Zhang, J.; Han, X.; Li, Q. F.; Wang, Z. L.; Wei, R. H. Corrosion and salt scale resistance of multilayered diamond-like carbon film in CO2 saturated solutions. *Corros. Sci.* **2014**, *86*, 261−267.
(44) Vedalakshmi, R.; Saraswathy, V.; Song, H. W.; Palaniswamy, N. Determination of diffusion coefficient of chloride in concrete using Warburg diffusion coefficient. *Corros. Sci.* **2009**, *51* (6), 1299−1307.
(45) Li, H.; Liu, L.; Guo, P.; Sun, L.; Wei, J.; Liu, Y.; Li, S.; Wang, S.; Lee, K.-R.; Ke, P.; Wang, A. Long-term tribocorrosion resistance and failure tolerance of multilayer carbon-based coatings. *Friction* **2022**, *10* (10), 1707−1721.
(46) Rudenja, S.; Pan, J.; Wallinder, I. O.; Leygraf, C.; Kulu, P. Passivation and anodic oxidation of duplex TiN coating on stainless steel. *J. Electrochem. Soc.* **1999**, *146* (11), 4082−4086.
(47) Wei, J.; Guo, P.; Liu, L.; Li, H.; Li, H.; Wang, S.; Ke, P.; Saito, H.; Wang, A. Corrosion resistance of amorphous carbon film in 3.5 wt % NaCl solution for marine application. *Electrochim. Acta* **2020**, *346*, 136282.
(48) Qiu, S.; Li, W.; Zheng, W.; Zhao, H.; Wang, L. Synergistic Effect of Polypyrrole-Intercalated Graphene for Enhanced Corrosion Protection of Aqueous Coating in 3.5% NaCl Solution. *ACS Appl. Mater. Interfaces* **2017**, *9* (39), 34294−34304.
(49) Trinh, D.; Dauphin Ducharme, P.; Mengesha Tefashe, U.; Kish, J. R.; Mauzeroll, J. Influence of edge effects on local corrosion rate of magnesium alloy/mild steel galvanic couple. *Anal. Chem.* **2012**, *84* (22), 9899−9906.
(50) Xie, J.; Komvopoulos, K. The effect of Argon ion irradiation on the thickness and structure of ultrathin amorphous carbon films. *J. Appl. Phys.* **2016**, *119* (9), 095304.
(51) Cuomo, J. J.; Doyle, J. P.; Bruley, J.; Liu, J. C. Sputter deposition of dense diamond-like carbon films at low temperature. *Appl. Phys. Lett.* **1991**, *58* (5), 466−468.
(52) Robertson, J. Diamond-like amorphous carbon. *Mater. Sci. Eng. R Rep.* **2002**, *37* (4−6), 129−281.
(53) Liu, Z.; Wang, Z.; Deng, Y.; Hu, W.; Xia, D.-H.; Tribollet, B. Accelerated corrosion mechanism of AA5083 coupled with Al-Zn-In anodes: An impedance analysis. *Corros. Sci.* **2026**, *258*, 113448.
(54) Liu, Z.; Yao, X.; Qin, Z.; Tribollet, B.; Xia, D. H. Corrosion Failure Analysis of AA5083 Connected With Al-Zn-In-Cd Anode in Simulated Seawater Level Fluctuation Zone. *Mater. Corros.* **2026**, *77* (4), 583−595.

https://doi.org/10.1021/acsami.6c03124
ACS Appl. Mater. Interfaces 2026, 18, 36164−36176